J. Phys.: Condens. Matter 4 (1992) 8783–8800. Printed in the UK

Three-dimensional numerical analysis of multi-mode quantum transport in zero-dimensional resonant tunnelling diodes

Hiroshi Mizuta†, Chris Goodings‡, Mathias Wagner† and Shirun Ho†
† Hitachi Central Research Laboratory, Hitachi Ltd, Kokubunji, Tokyo 185, Japan
‡ Microelectronics Research Centre, University of Cambridge, Cambridge CB3 0HE, UK

Received 18 May 1992, in final form 28 July 1992

Abstract. Lateral-mode-non-conserving resonant tunnelling through a zero-dimensional AlGaAs/InGaAs/AlGaAs resonant tunnelling diode (0D RTD) has been analysed by numerically solving the three-dimensional Schrödinger equation with scattering boundary conditions. The multi-mode scattering matrix (S-matrix) method has been introduced for the first time to simulate the virtually confined electronic states and multi-mode quantum transport properties of the 0D RTD. We report on the effect of lateral-mode mixing, caused by elastic scattering due to an hour-glass-shaped confinement potential, on the multi-mode transmission properties and current–voltage characteristics of the device. The calculated S-matrix clearly shows both new transmission peaks in the off-diagonal components which measure the lateral-mode-non-conserving resonant tunnelling and the related Fano-resonance-type structures in the diagonal components which represent an interference between the second-order resonant tunnelling process and the conventional tunnelling process for the off-resonant condition. The total tunnelling current through the device is calculated and compared with results for a device with uniform lateral confinement. The difference between the energy separations of the lateral modes in the cathode region and in the quantum box leads to observable fine current peaks in the current–voltage characteristics due to the lateral-mode-conserving tunnelling. In addition, two small satellite peaks can be found in the high-voltage regime which originate in the lateral-mode-non-conserving tunnelling.

1. Introduction

Recent rapid advances in crystal growth and microfabrication techniques have allowed us to explore a new field of semiconductor device research. The quantum mechanical wave nature of electrons appears in mesoscopic semiconductor structures with sizes below 100 nm. Instead of conventional devices such as field effect transistors and bipolar transistors, which can be described by the classical model, a variety of novel device concepts have been proposed based on the quantum mechanical features of carriers. One pioneering device in this field is the resonant tunnelling diode (RTD) [1] which utilizes the electron wave resonance in a finite superlattice. The negative differential resistance obtained in these structures leads to multi-stable device operation, and several new devices have been successfully developed. Very recently, low-dimensional resonant tunnelling structures [2–9] in which electrons are confined laterally as well as vertically have become of great interest. Some experimental results have been reported on one-dimensional (1D) RTDs [4, 6] and zero-dimensional

0953-8984/92/458783+18$07.50

(0D) RTDs [2–5, 7–9]. The 0D RTD (see figure 1) is a virtually isolated quantum dot only weakly coupled to reservoirs and so is well suited to investigating electron wave transport properties through three-dimensionally quantized energy levels. By designing structural parameters such as barrier thickness, quantum well width, and dimensions of lateral confinement, it is now possible to realize a 'quantum box' in which the number of electrons is nearly quantized, so the effect of single-charge-assisted transport, or so-called Coulomb blockade [10–12], becomes significant.

Experimental results reported so far show quite clear fine structure in the current–voltage characteristics even at rather high temperatures ($\sim$ 77 K) superimposed on the usual negative differential resistance of 2D RTDs. The mechanism of this fine structure is under active discussion and several theoretical investigations have been reported [13–16]. The difficulty in analysing electron transport in this system stems from the non-uniform lateral-confinement potential which is formed by differences in surface depletion, even though the device is fabricated to be geometrically straight in a vertical direction. As long as the lateral-confinement potential is uniform throughout a device [13], an electron wave tunnels through a given channel without coupling to other channels. Non-uniform confinement, however, causes lateral wavefunction mismatch and changes transport from independent channel tunnelling to coupled channel tunnelling. Bryant [14–16] reported on theoretical analyses of 0D RTDs which took account of lateral-mode mixing by assuming a constant mixing parameter, and showed that new current peaks appeared which depended on the strength of mode mixing. Reed and co-workers [3, 17] explained his experimental data by assuming sequential electron tunnelling from quantized lateral levels in the emitter region to quantum dot levels in the well. They concluded that the observed fine peaks were attributable to tunnelling in which lateral momentum is not conserved. Further quantitative analysis, however, obviously requires numerical calculations based on the three-dimensional scattering theory, which fully includes lateral-mode mixing.

The purpose of this work is to present a theoretical analysis of quantum transport in 0D RTDs based on numerical solutions of the three-dimensional Schrödinger equation for open systems. Several theoretical studies of the two-dimensional scattering equation have been reported for laterally patterned two-dimensional electron gas systems [18–25]. Because direct numerical calculations usually have large computational time and memory requirements, several useful alternative methods have also been proposed. Also, the three-dimensional Schrödinger equation has been solved by Kumar and co-workers for a completely isolated quantum dot under a magnetic field [26] and a structure periodic in one direction [27]. Since the electronic states become completely bound states or sub-bands rather than continuous scattering states in these circumstances, this method is not adequate for the present purpose. Very recently, Nakasato and Blaikie [28] have analysed transport properties of lateral quantum wires with geometrical confinement by solving the two-dimensional scattering equation numerically, and have shown anti-resonance dips of conductance resulting from lateral-mode mixing. In this paper we present the three-dimensional scattering formulation and calculate the scattering matrix (S-matrix) numerically to investigate the effect of two-dimensional lateral-mode mixing on the transport properties of 0D RTDs. In the present calculation the self-consistent Hartree potential, which would be crucial for analysing the Coulomb blockade, is neglected for simplicity. In the next section we present our formulation based on three-dimensional scattering theory. In section 3 the present theory is applied to the laterally confined 0D AlGaAs/InGaAs/AlGaAs resonant tunnelling diodes. The hour-

glass-shaped confinement potential due to surface Fermi-level pinning is calculated in advance using a classical device simulation with the Spicer *et al* surface defect model [30]. This potential is then applied to the three-dimensional Schrödinger equation. We focus on the effect of lateral-mode mixing, caused by elastic scattering due to the hour-glass-shaped confinement potential, on the multi-mode transmission properties and current–voltage characteristics of the device. The S-matrix is calculated to analyse momentum-non-conserving tunnelling which can be observed in the off-diagonal components of the transmission probability. Furthermore a total tunnelling current through the device is calculated and compared with results for a device with uniform lateral confinement, in order to investigate the mechanism of the fine structure in the current–voltage characteristics.

2. Three-dimensional S-matrix theory

In this section the formulation of multi-mode quantum transport in the 0D RTD is described based on a three-dimensional S-matrix theory. We start from the three-dimensional time-independent Schrödinger equation:

$$-(\hbar^2/2m^*)(\partial^2/\partial x^2 + \partial^2/\partial y^2 + \partial^2/\partial z^2)\Psi(x, y, z) + V(x, y, z)\Psi(x, y, z) = E\Psi(x, y, z) \tag{1}$$

where m^* is the conduction band effective mass and $V(x, y, z)$ is the three-dimensional potential distribution which consists of the electron affinity $V_0(x, y, z)$, the lateral-confinement potential $V_{LC}(x, y, z)$, and the potential due to an external bias $V_{EX}(x, y, z)$:

$$V(x, y, z) = V_0(x, y, z) + V_{LC}(x, y, z) + V_{EX}(x, y, z). \tag{2}$$

The three-dimensional wavefunction $\Psi(x, y, z)$ is decomposed by using a complete set of two-dimensional lateral wavefunctions at each z-point, $\varphi_\gamma(x, y \mid z)$, as follows:

$$\Psi(x, y, z) = \sum_\gamma \varphi_\gamma(x, y \mid z)\chi_\gamma(z). \tag{3}$$

The lateral wavefunction $\varphi_\gamma(x, y \mid z)$ is obtained by solving numerically the following two-dimensional Schrödinger equation:

$$-(\hbar^2/2m^*)(\partial^2/\partial x^2 + \partial^2/\partial y^2)\varphi_\gamma(x, y \mid z) + V(x, y, z)\varphi_\gamma(x, y \mid z) = \epsilon_\gamma(z)\varphi_\gamma(x, y \mid z) \tag{4}$$

with the Dirichlet boundary conditions, $\varphi_\gamma(x, y \mid z) = 0$, on the boundaries of the device. The index γ represents a two-dimensional lateral-mode number and $\epsilon_\gamma(z)$ a corresponding γth lateral eigen-energy.

Substituting equation (3) into equation (1), the three-dimensional Schrödinger equation reduces to the following one-dimensional scattering equation for the z-component of the wavefunction $\chi_\gamma(z)$:

$$\frac{d^2}{dz^2}\chi_\gamma(z) + k_\gamma^2(z)\chi_\gamma(z) + \sum_{\gamma'}\left(2C_{\gamma,\gamma'}^{(0,1)}(z)\frac{d}{dz}\chi_{\gamma'}(z) + C_{\gamma,\gamma'}^{(0,2)}(z)\chi_{\gamma'}(z)\right) = 0 \tag{5}$$

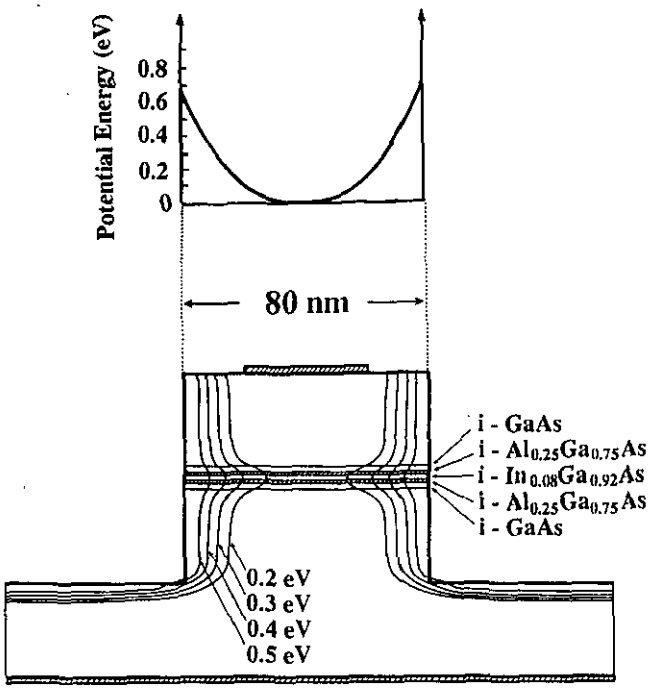

Figure 1. Lateral-confinement potential distribution in the zero-dimensional AlGaAs/InGaAs/AlGaAs resonant tunnelling diode, calculated by using a classical device simulation taking account of the surface carrier trap levels.

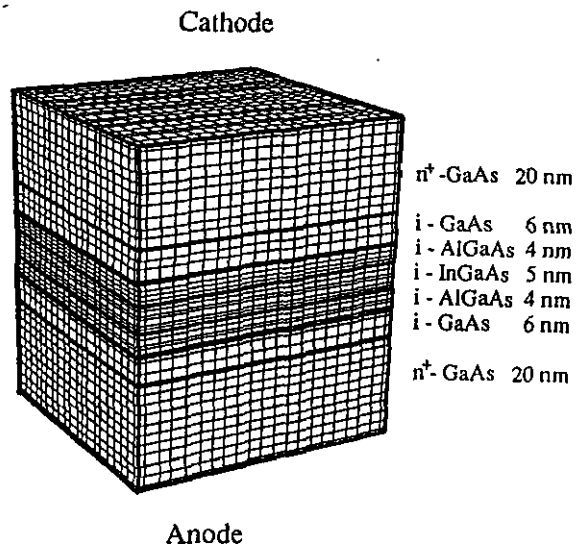

Figure 2. Three-dimensional finite-difference mesh lattice used for numerical calculations. The mesh spacing has been chosen to be small for the AlGaAs barriers and the GaAs quantum well.

where $k_\gamma(z)$ denotes a complex wavenumber given by

$$k_\gamma^2(z) = (2m^*/\hbar^2)(E - \epsilon_\gamma(z)). \tag{6}$$

Mode mixing coefficients $C_{\gamma,\gamma'}^{(0,1)}$ and $C_{\gamma,\gamma'}^{(0,2)}$ are written as

$$C_{\gamma,\gamma'}^{(0,1)}(z) = \int \mathrm{d}x \int \mathrm{d}y\, \varphi_\gamma(x, y \mid z) \frac{\partial}{\partial z} \varphi_{\gamma'}(x, y \mid z) \tag{7}$$

$$C_{\gamma,\gamma'}^{(0,2)}(z) = \int \mathrm{d}x \int \mathrm{d}y\, \varphi_\gamma(x, y \mid z) \frac{\partial^2}{\partial z^2} \varphi_{\gamma'}(x, y \mid z) \tag{8}$$

and are evaluated by using the previously obtained set of lateral wavefunctions. The third term in equation (5) causes the mixing of lateral modes and is non-zero unless the system is uniform in the z-direction. The first-derivative term of $\chi_\gamma(z)$ in (5) can be eliminated by applying the unitary transformation:

$$\chi_\gamma(z) = \sum_{\gamma'} M_{\gamma,\gamma'}(z) f_{\gamma'}(z) \tag{9}$$

where a unitary matrix $M_{\gamma\gamma'}(z)$ is defined as follows:

$$M_{\gamma,\gamma'}(z) = \exp\left(- \int^z C_{\gamma,\gamma'}^{(0,1)}(z')\, \mathrm{d}z' \right). \tag{10}$$

The matrix $M_{\gamma\gamma'}(z)$ is calculated by using a second-order-expansion approximation [28] which guarantees unitarity of the matrix. Substituting equations (9) and (10) into equation (5), the transformation leads to the following equation:

$$\frac{\mathrm{d}^2}{\mathrm{d}z^2} f_\gamma(z) = - \sum_{\gamma'} \omega_{\gamma,\gamma'}(z) f_{\gamma'}(z) \tag{11}$$

where a matrix $\omega_{\gamma\gamma'}(z)$ is written as

$$\omega_{\gamma,\gamma'}(z) = \sum_{\gamma''} \sum_{\gamma'''} (\mathbf{M}^{-1})_{\gamma,\gamma''}(z) W_{\gamma'',\gamma'''}(z) M_{\gamma''',\gamma'}(z) \tag{12}$$

$$W_{\gamma,\gamma'}(z) = k_\gamma^2(z)\delta_{\gamma,\gamma'} - \left\{ C^{(0,1)}(z) \right\}_{\gamma,\gamma'}^2 - C_{\gamma,\gamma'}^{(1,1)}(z) \tag{13}$$

$$C_{\gamma,\gamma'}^{(1,1)}(z) = \int \mathrm{d}x \int \mathrm{d}y \frac{\partial}{\partial z} \varphi_\gamma(x, y \mid z) \frac{\partial}{\partial z} \varphi_{\gamma'}(x, y \mid z) \tag{14}$$

and the expression $\{C^{(0,1)}(z)\}_{\gamma,\gamma'}^2$ in equation (13) means the (γ, γ') element of the multiplied matrix $C^{(0,1)}(z)C^{(0,1)}(z)$.

A set of renormalized complex wavenumbers $K_\gamma(z)$, which takes in the lateral-mode mixing, is obtained by solving an eigenvalue equation:

$$\sum_{\gamma''} W_{\gamma,\gamma''}(z) V_{\gamma'',\gamma'}(z) = \{K_{\gamma'}(z)\}^2 V_{\gamma,\gamma'}(z) \tag{15}$$

where $V_{\gamma\gamma'}(z)$ is a unitary matrix which diagonalizes the matrix $W_{\gamma\gamma'}(z)$. Then the z-component of the wavefunction can be expressed as a superposition of plane waves:

$$\chi_\gamma(z) = \sum_{\gamma'}\sum_{\gamma''} M_{\gamma,\gamma'}(z)V_{\gamma',\gamma''}(z)\left\{A_{\gamma''}(z)\exp(\mathrm{i}K_{\gamma''}(z)z)\right.$$
$$\left. + B_{\gamma''}(z)\exp(-\mathrm{i}K_{\gamma''}(z)z)\right\} \tag{16}$$

where $A_\gamma(z)$ and $B_\gamma(z)$ are coefficients of forward and backward plane waves in the γth lateral mode with the complex wavenumber $K_\gamma(z)$. Equation (16) is discretized on the finite-difference z-mesh points (see figure 2). Assuming these coefficients to be constant between two adjacent z-mesh points, the three-dimensional wavefunction $\Psi(x, y, z)$ can be finally written as

$$\Psi^{(i)}(x, y, z) \cong \sum_{\gamma}\sum_{\gamma'}\sum_{\gamma''} \varphi_\gamma(x, y \mid z)M^{(i)}_{\gamma,\gamma'}V^{(i)}_{\gamma',\gamma''}\left\{A^{(i)}_{\gamma''}\exp(\mathrm{i}K^{(i)}_{\gamma''}z)\right.$$
$$\left. + B^{(i)}_{\gamma''}\exp(-\mathrm{i}K^{(i)}_{\gamma''}z)\right\} \tag{17}$$

where the index (i) denotes a small region between adjacent z-mesh points z_i and z_{i+1}.

From the continuity of the probability flux of electrons through the system, the following conditions on the total wavefunctions hold at the z-mesh point z_{i+1} for given x and y:

$$\Psi^{(i)}(x, y, z_{i+1}) = \Psi^{(i+1)}(x, y, z_{i+1}) \tag{18}$$

$$(1/m^*)(\partial/\partial z)\Psi^{(i)}(x, y, z)\big|_{z=z_{i+1}} = (1/m^*)(\partial/\partial z)\Psi^{(i+1)}(x, y, z)\big|_{z=z_{i+1}}. \tag{19}$$

The coefficients at the adjacent z-mesh points are then related as follows:

$$\begin{pmatrix} A^{i+1}_\gamma \\ B^{i+1}_\gamma \end{pmatrix} = \sum_{\gamma'} \mathsf{T}^{(i)}(\gamma,\gamma')\begin{pmatrix} A^{i}_{\gamma'} \\ B^{i}_{\gamma'} \end{pmatrix}. \tag{20}$$

The matrix $\mathsf{T}^{(i)}(\gamma,\gamma')$ can be expressed as

$$\mathsf{T}^{(i)}(\gamma,\gamma') = \begin{pmatrix} \alpha^{(i)}_+(\gamma,\gamma')P & \alpha^{(i)}_-(\gamma,\gamma')/Q \\ \alpha^{(i)}_-(\gamma,\gamma')Q & \alpha^{(i)}_+(\gamma,\gamma')/P \end{pmatrix} X^{(i)}_{\gamma,\gamma'} \tag{21}$$

where P stands for $\exp\{\mathrm{i}(K^{(i)}_{\gamma'} - K^{(i+1)}_{\gamma})z_{i+1}\}$ and Q stands for $\exp\{\mathrm{i}(K^{(i)}_{\gamma'} + K^{(i+1)}_{\gamma})z_{i+1}\}$, and where matrix elements $\alpha^{(i)}_\pm(\gamma,\gamma')$ and $X^{(i)}_{\gamma,\gamma'}$ are given by the following expressions:

$$\alpha^{(i)}_\pm(\gamma,\gamma') = \tfrac{1}{2}\left(1 \pm (m^*_{i+1}/m^*_i)(K^{(i)}_{\gamma'}/K^{(i+1)}_{\gamma})\right) \tag{22}$$

$$X^{(i)}_{\gamma,\gamma'} = \sum_{\gamma_1}\sum_{\gamma_2}\sum_{\gamma_3} V^{(i+1)}_{\gamma_1,\gamma}M^{(i+1)}_{\gamma_2,\gamma_1}M^{(i)}_{\gamma_2,\gamma_3}V^{(i)}_{\gamma_3,\gamma'}. \tag{23}$$

Hence the coefficients at the cathode (A_γ^{L}, B_γ^{L}) and anode (A_γ^{R}, B_γ^{R}) edges of the device are related by using a multi-mode transfer matrix $\mathbf{T}(\gamma, \gamma')$:

$$\begin{pmatrix} A_\gamma^{\mathrm{L}} \\ B_\gamma^{\mathrm{L}} \end{pmatrix} = \sum_{\gamma'} \mathbf{T}(\gamma, \gamma') \begin{pmatrix} A_{\gamma'}^{\mathrm{R}} \\ B_{\gamma'}^{\mathrm{R}} \end{pmatrix} \tag{24}$$

$$\mathbf{T} = \mathbf{T}^{(N)}\mathbf{T}^{(N-1)}\mathbf{T}^{(N-2)} \ldots \mathbf{T}^{(2)}\mathbf{T}^{(1)}. \tag{25}$$

It should be noted that the transfer matrix contains both propagating and evanescent modes depending on the total energy and lateral-mode eigen-energies. Nakasato and Blaikie [28] calculated a reduced transfer matrix from the above full transfer matrix, to separate the propagating modes from the evanescent ones. In the present calculations, however, there is always a difference in the number of propagating modes at the cathode and anode edges under a non-zero external bias, and the resultant reduced transfer matrix is no longer regular. Thus in the following calculations the full transfer matrix is adopted rather than the reduced transfer matrix. A relevant multi-mode scattering matrix $\mathbf{S}(\gamma, \gamma')$ which is defined as

$$\begin{pmatrix} B_\gamma^{\mathrm{L}} \\ A_\gamma^{\mathrm{R}} \end{pmatrix} = \sum_{\gamma'} \mathbf{S}(\gamma, \gamma') \begin{pmatrix} A_{\gamma'}^{\mathrm{L}} \\ B_{\gamma'}^{\mathrm{R}} \end{pmatrix} \tag{26}$$

is calculated from the transfer matrix. The multi-mode transmission probability $t_{\mathrm{L,R}}(E; \gamma, \gamma')$ and the total transmission rate $T(E)$, i.e. conductance at zero temperature, are then obtained from the S-matrix as follows:

$$t_{\mathrm{R}}(E; \gamma, \gamma') = |S_{12}(\gamma, \gamma')|^2 \tag{27}$$

$$t_{\mathrm{L}}(E; \gamma, \gamma') = |S_{21}(\gamma, \gamma')|^2 \tag{28}$$

$$\begin{aligned} T(E) &= \sum_{\gamma} \sum_{\gamma'} t_{\mathrm{R}}(E; \gamma, \gamma') \theta(E - \epsilon_\gamma^{\mathrm{L}}) \theta(E - \epsilon_{\gamma'}^{\mathrm{R}}) \\ &= \sum_{\gamma} \sum_{\gamma'} t_{\mathrm{L}}(E; \gamma, \gamma') \theta(E - \epsilon_\gamma^{\mathrm{L}}) \theta(E - \epsilon_{\gamma'}^{\mathrm{R}}) \end{aligned} \tag{29}$$

where $\theta(E)$ is the step function. A complete set of the three-dimensional wavefunctions $\Psi(x, y, z)$ can be obtained by using the following scattering boundary conditions:

$$(A_\gamma^{\mathrm{L}}, B_\gamma^{\mathrm{R}}) = (\delta_{\gamma,\gamma_0}, 0) \qquad (\gamma = 1, 2, 3, \ldots) \tag{30}$$

for an incident electron wave with a lateral mode γ_0 originating at the cathode edge of the system, and

$$(A_\gamma^{\mathrm{L}}, B_\gamma^{\mathrm{R}}) = (0, \delta_{\gamma,\gamma_0}) \qquad (\gamma = 1, 2, 3, \ldots) \tag{31}$$

when it originates at the anode edge. In equations (30) and (31) δ_{γ,γ_0} is the delta function. If the system has a real bound state which may be caused by an attractive scatterer such as an InGaAs quantum well or a deep donor trap level, a bound state problem has to be solved as well as the above scattering state problem to obtain a complete set of wavefunctions. Finally, the total tunnelling current I_{tunnel} is calculated assuming global coherent tunnelling of electron waves throughout the device as follows:

$$I_{\mathrm{tunnel}} = \frac{e}{\pi\hbar} \int_{eV}^{\infty} T(E)\{f_{\mathrm{L}}(E) - f_{\mathrm{R}}(E)\}\,\mathrm{d}E \tag{32}$$

where $f_{\mathrm{L}}(E)$ and $f_{\mathrm{R}}(E)$ are Fermi distribution functions in the cathode and anode regions, respectively.

3. Numerical results and discussions

In this section the three-dimensional scattering theory described in the previous section is applied to the 0D RTD structure shown in figure 1, and multi-mode quantum transport is analysed numerically. In the present paper we adopt a laterally confined AlGaAs/InGaAs/AlGaAs double-barrier resonant tunnelling structure. The assumed layer structure consists of an undoped $In_{0.08}Ga_{0.92}As$ quantum well of 5 nm in thickness, two undoped $Al_{0.25}Ga_{0.75}As$ barriers of 4 nm in thickness, two undoped GaAs spacer layers of 6 nm in thickness, and n^+-type GaAs cathode and anode layers with a donor concentration of 1.0×10^{18} cm^{-3}. The conduction band discontinuities in the $GaAs/Al_{0.25}Ga_{0.75}As$ and $GaAs/In_{0.08}Ga_{0.92}As$ heterostructures are assumed to be 187.0 and -37.2 meV, respectively. The electron effective mass in the GaAs, $Al_{0.25}Ga_{0.75}As$, and $In_{0.08}Ga_{0.92}As$ layers is assumed to be 0.067, 0.088, and $0.064m_0$, respectively. Lateral dimensions of the device are set to be 80 nm in both x- and y-dimensions.

The first part of the numerical simulation is to obtain a realistic lateral-confinement potential distribution created by carrier trap levels on the lateral surface. The exact lateral-confinement potential should be determined through a fully self-consistent calculation of the three-dimensional Schrödinger equation. However, this would require an enormous amount of computational time and is beyond our present requirements. The self-consistent calculations are left for a future analysis of Coulomb blockade tunnelling where the self-consistent field produced by a single electron is dominant. In the present work the confinement potential is calculated by using a classical device simulation [29] in which surface carrier traps are taken into consideration by using the Spicer *et al* unified defect model [30]: a deep donor level at 0.925 eV measured from the conduction band edge and a deep acceptor level at 0.75 eV from the valence band edge are assumed on the GaAs lateral surface. As long as the size of the lateral confinement is much larger than the width of the quantum well, the calculated potential distribution should be a fairly good approximation for the exact potential distribution determined by the self-consistent calculation. Figure 1 shows the calculated potential distribution where the sheet concentration of the surface deep level is assumed to be 5.0×10^{12} cm^{-2}, which is a plausible value large enough to pin the Fermi level on the surface. It can be seen that the hour-glass-shaped confinement potential results from the different surface depletion widths in the intrinsic and contact regions.

The second part of the simulation is to calculate the lateral eigen-energies and two-dimensional eigenstates at each z-point by using the hour-glass confinement potential. Equation (4) is discretized by using a three-dimensional finite-difference mesh lattice, shown in figure 2, which has a uniform mesh spacing in the x- and y-dimensions and a non-uniform spacing in the z-dimension. Eigen-energies of the resultant finite-difference equation are obtained up to a given value of total energy by using the bisection method following Householder's tridiagonalization. The corresponding eigenvectors are then calculated by the inverse iteration method. To speed up finding the eigenvectors, the set of eigenstates obtained at the previous z-mesh point is used as an initial guess for the eigenstates at the next z-mesh point. For numerical calculations a cut-off value is introduced for the maximum eigen-energy although all of the lateral modes would be necessary to make a complete set. The number of wavefunctions required for realistic calculations depends on the system under consideration. In general at least all of the lateral eigenstates with

eigen-energies below the Fermi energy should be taken into account. In the present calculations, for instance, there are four lateral eigenstates below the Fermi level and 13 lateral modes are calculated for all z-mesh points.

By making use of the lateral eigenstates, the mixing coefficients, $C^{(0,1)}_{\gamma,\gamma'}$ and $C^{(0,2)}_{\gamma,\gamma'}$, and the unitary transformation matrix, $M_{\gamma\gamma'}(z)$, can be evaluated from equations (7), (8) and (10). The eigenvalue equation (15) is then solved to get the renormalized wavenumbers, $K_\gamma(z)$, and the unitary matrix, $V_{\gamma\gamma'}(z)$. As the matrix $W_{\gamma\gamma'}(z)$ is real and symmetric, all of the eigenvalues and eigenvectors can be obtained by using the QL method [31]. Finally, by using the lateral eigenstates at the cathode and anode edges, the multi-mode transfer matrix and the resultant scattering matrix are calculated from equations (21)–(27).

The multi-mode transmission probability calculated for the 0D RTD structure is shown in figure 3. Figure 3(*a*) shows the total energy dependence of transmission probability for diagonal tunnelling from the γth incident mode to the γth transmission mode, $|S_{12}(\gamma,\gamma)|^2$, and figure 3(*b*) that for off-diagonal tunnelling from the first incident mode to the γth transmission mode, $|S_{12}(1,\gamma)|^2$. The S-matrix elements are drawn for values of γ' up to 11. In addition, the transmission probability calculated for a device with completely uniform confinement is shown in figure 4. Before proceeding to the detailed discussion of these results, it is worth commenting on this structure. The uniform lateral confinement used for the calculation in figure 4 could be realized by doping the resonant tunnelling structure uniformly, as well as the contact regions. However, resonant tunnelling is hardly observed in such doped structures because resonant electron waves suffer from frequent impurity scattering in the quantum well. Thus the results in figure 4 are based on an unrealistic assumption that electron waves travel ballistically even in a doped tunnelling structure, and are given simply for comparison with the results for the hour-glass confinement. In figure 4 the S-matrix has no off-diagonal elements since there is no lateral wavefunction mismatch anywhere in the system. This is called independent channel tunnelling, as the lateral modes are not mixed. The total transmission rate is then just a superposition of the transmission probabilities through these independent channels shown as a thick full curve in figure 4. Electronic states corresponding to the first three transmission probability peaks in figure 4 are shown in figures 5(*a*)–(*d*). These figures show the visualized three-dimensional existence probability of electrons, $|\Psi_E(x, y, z)|^2$, in the device: (*a*) $|\Psi_E(x, y, z)|^2$ for the tunnelling process from the first mode at the cathode edge to the first mode at the anode edge (this is hereafter denoted as $1 \rightarrow 1$) at the first peak energy, (*b*) for the process $2 \rightarrow 2$ at the second peak energy, (*c*) for the process $3 \rightarrow 3$ at the second peak energy, and (*d*) for the process $4 \rightarrow 4$ at the third peak energy. It should be noted that the wavefunctions for these states are virtually localized in the quantum box and clearly reflect eigenstates of the quantum box itself. This fact means that the lateral-mode index γ is a good quantum number throughout the device.

On the other hand, the following two major differences can be seen in the tunnelling properties of the hour-glass confinement shown in figure 3. First, the energy intervals between transmission probability peaks become larger than those in figure 4, leading to a large peak-to-valley ratio of transmission probability. Second, the elastic scattering due to the hour-glass confinement potential mixes the lateral modes and opens new off-diagonal tunnelling channels. In figure 3(*b*) two peaks can be found in the off-diagonal elements of the S-matrix which represent lateral-mode-non-conserving resonant tunnelling. It should be noted that off-diagonal tunnelling with

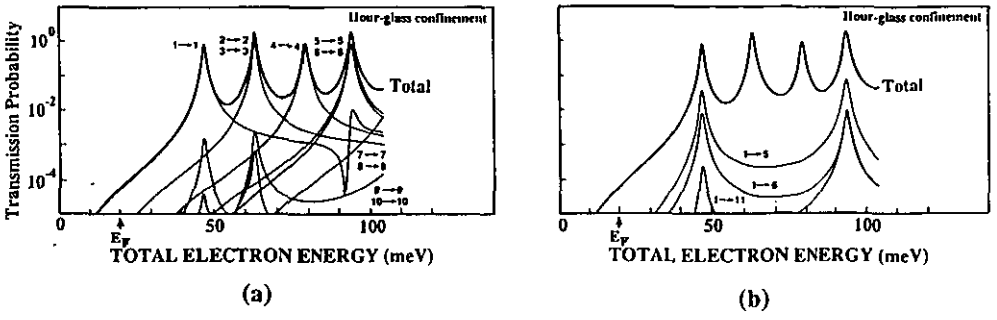

Figure 3. Multi-mode transmission probability $|S_{12}(\gamma, \gamma')|^2$ calculated for the 0D RTD structure with hour-glass lateral confinement: (*a*) total energy dependence of transmission probability for diagonal tunnelling from the γth incident mode to the γth transmission mode, $|S_{12}(\gamma, \gamma)|^2$, and (*b*) that for off-diagonal tunnelling from the first incident mode to the γth transmission mode, $|S_{12}(1, \gamma)|^2$. The S-matrix elements are drawn for values of γ' up to 11. A thick full curve represents the total transmission probability $T(E)$ defined by equation (29).

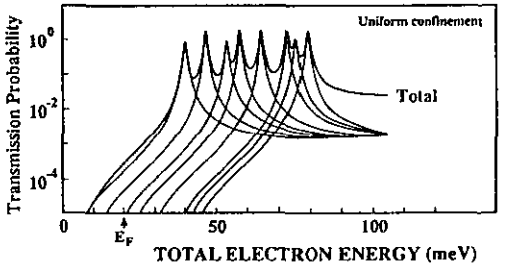

Figure 4. Multi-mode transmission probability $|S_{12}(\gamma, \gamma)|^2$ calculated for the 0D RTD structure with uniform lateral confinement. The off-diagonal elements are now zero.

the first incident mode is observed only for the fifth, sixth, and eleventh transmission modes. This is purely because of a selection rule for parity of lateral wavefunctions. Because the elastic scattering due to the hour-glass confinement potential does not break symmetry under mirror reflection in x- and y-dimensions, a lateral mode couples only with other modes having the same parity. The lowest wavefunction has even parities in both x- and y-dimensions, and can therefore couple only with upper modes described above. Additional structures are also observed in the diagonal elements in figure 3(*a*). For example, an asymmetric resonant structure can be seen at a total energy of 91.7 meV. It should be noted that the off-diagonal tunnelling probability is quite large for the process $1 \rightarrow 5$ at this energy. In these circumstances the ratio of the second-order diagonal tunnelling is enhanced, in which two elastic scattering events are involved between the first and fifth lateral modes: this is shown diagrammatically in figure 6(*b*). This process is now at resonance and interferes with the major diagonal tunnelling process, shown in figure 6(*a*), which is at off-resonance. The interaction between these two tunnelling processes results in the Fano-resonance-type lineshape in the transmission probability [32]. The three-dimensional existence probability of electrons, $|\Psi_E(x, y, z)|^2$ at the energy of 91.7 meV is shown in figure 7. It should be noted that the electron existence probability in the quantum box reflects features of the fifth mode rather than the first mode despite the first-mode nature of

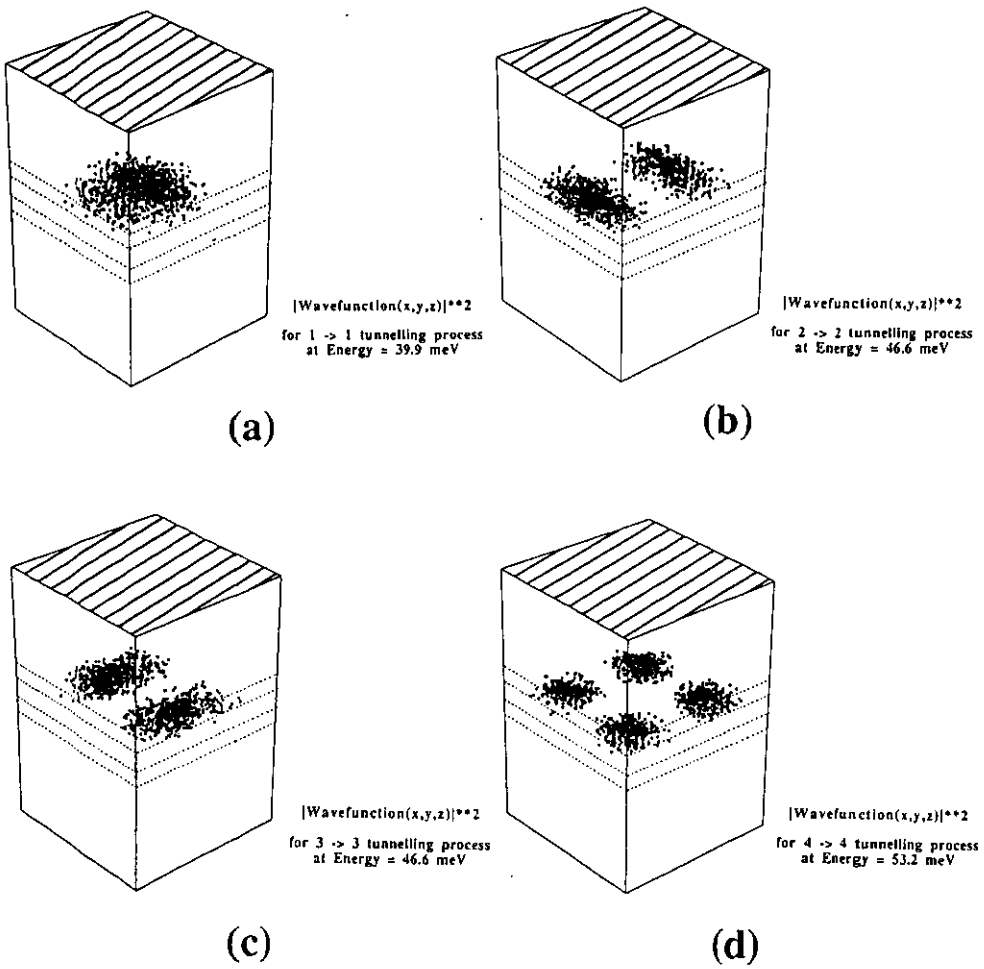

Figure 5. Visualized three-dimensional existence probability of electrons $|\Psi_E(x, y, z)|^2$ at the lowest three transmission peaks in figure 4: (*a*) $|\Psi_E(x, y, z)|^2$ for the process $1 \rightarrow 1$ at the first peak energy; (*b*) for the process $2 \rightarrow 2$ at the second peak energy; (*c*) for the process $3 \rightarrow 3$ at the second peak energy; and (*d*) for the process $4 \rightarrow 4$ at the third peak energy. It should be noted that the second peak in figure 4 is caused by both tunnelling processes $2 \rightarrow 2$ and $3 \rightarrow 3$. It can be seen that the electron distribution clearly reflects the lateral eigenstates in the quantum box.

the incoming wave. This signifies that a large part of the incoming wave is converted to the fifth mode in the quantum box through experiencing lateral-mode-non-conserving perturbation due to the change in the lateral confinement. In these circumstances the lateral-mode index γ is no longer a good quantum number for the system.

The applied voltage dependence of the total tunnelling current is calculated by assuming ballistic transport throughout the device (equation (32)). Figure 8(*a*) shows the I–V characteristics of the device with the hour-glass lateral confinement calculated at a temperature of 77 K. Uniform external electric field is assumed in the intrinsic regions of the device in this calculation. Several satellite current peaks

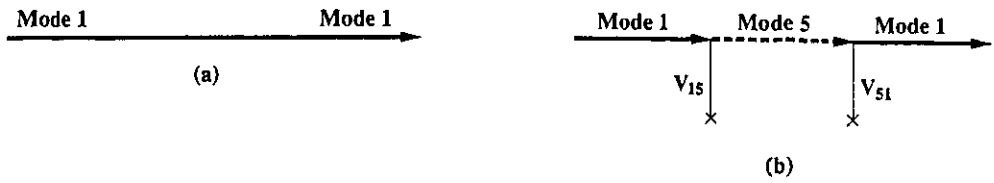

Figure 6. Diagrammatic representation of two processes involved in the diagonal tunnelling, $1 \rightarrow 1$, at Fano resonance: (*a*) zero-order tunnelling and (*b*) second-order tunnelling. V_{51} and V_{15} denote the elastic scattering between the first and the fifth lateral modes due to an hour-glass confinement potential.

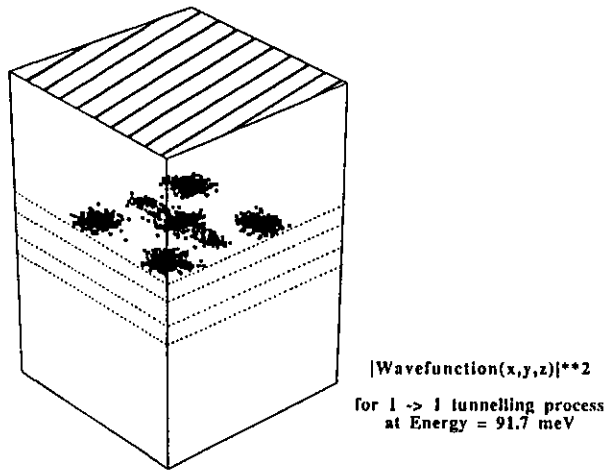

Figure 7. Visualized three-dimensional existence probability of electrons $|\Psi_E(x, y, z)|^2$ for the tunnelling process $1 \rightarrow 1$ at an energy of 91.7 meV which corresponds to the dip of the Fano resonance in figure 3. It should be noted that the electron existence probability in the quantum box reflects features of the fifth mode rather than the first mode, despite the first-mode nature of the incoming wave.

and shoulders are observed superposed on the conventional negative conductance characteristics of 2D RTDs. Figure 8(*b*) shows the I–V characteristics calculated at lower temperatures. It can be seen that the fine structure in the I–V characteristics stands out more at a lower temperature. Also the current–voltage characteristics are compared with those of a device with uniform confinement (broken curve) in figure 9. It should be noted that only one major current peak is found without any fine structure in the case of uniform confinement, as the peak-to-valley ratio of the transmission probability shown in figure 4 is not large enough to separate the contribution from each mode. In the case of the hour-glass confinement, on the other hand, the following mechanisms lead to the observable small current peaks in figure 8. The total energy dependences of the transmission probabilities calculated at the first four peak (shoulder) voltages are shown in figures 10(*a*)–(*h*): the diagonal elements: $|S_{12}(\gamma, \gamma)|^2$, calculated at the first, second, third, and fourth peak voltages in figures 10(*a*), (*c*), (*e*), and (*g*) and the off-diagonal elements, $|S_{12}(1, \gamma)|^2$, in figures 10(*b*), (*d*), (*f*), and (*h*). The total transmission rate is shown by using thick

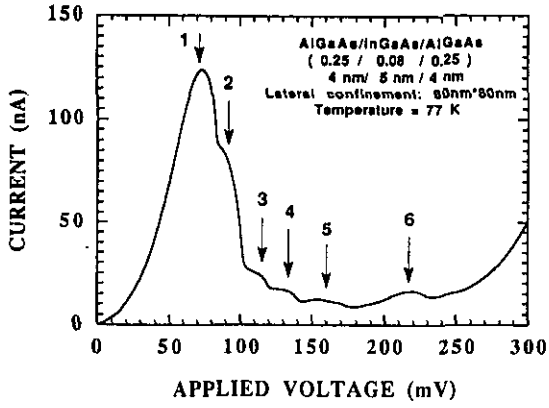

(a)

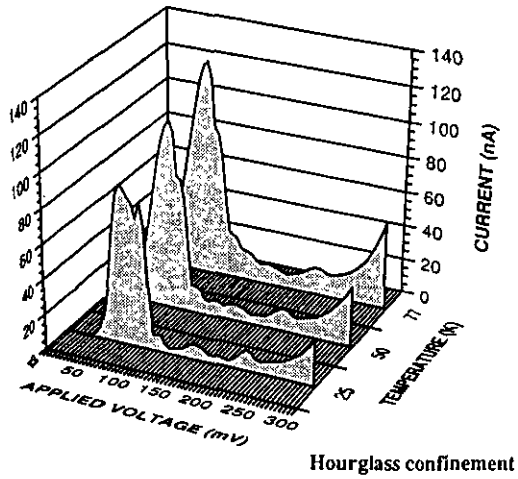

Hourglass confinement

(b)

Figure 8. (*a*) Applied voltage dependence of total tunnelling current calculated by using equation (32) at a temperature of 77 K. Observed satellite current peaks and shoulders are indicated by arrows. (*b*) The I–V characteristics calculated at lower temperatures.

full curves as in figures 3 and 4. The current peak (shoulder) appears each time the new transmission peak (indicated by an arrow) plunges into the Fermi sea. It can be seen that all of the four peaks are caused mainly by diagonal tunnelling (figures 10(*a*), (*c*), (*e*), and (*g*)) since the off-diagonal tunnelling shown in figures 10(*b*), (*d*), (*e*), and (*h*) contributes much less to the total transmission probability. Thus these four peaks mainly result from lateral-mode-conserving resonant tunnelling: $1 \rightarrow 1$ tunnelling for the first main peak, $2 \rightarrow 2$ and $3 \rightarrow 3$ for the second, $4 \rightarrow 4$ for the third, and $5 \rightarrow 5$ and $6 \rightarrow 6$ for the fourth. As shown in figure 8(*b*) the fourth peak becomes smaller with decreasing temperature since it is caused by the tunnelling of electrons which are thermally excited to the fifth and sixth modes located above the quasi-Fermi level in the cathode region. Obviously other higher diagonal channels such as the $7 \rightarrow 7$

and $8 \rightarrow 8$ play a negligibly small role since very few electrons occupy the higher eigenstates in the cathode region.

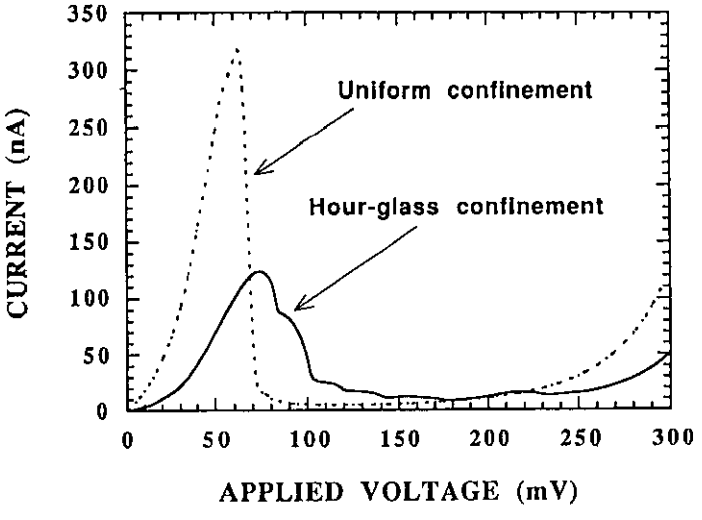

Figure 9. Comparison of the current–voltage characteristics calculated for the hour-glass confinement (full curve) with those for the uniform confinement (broken curve).

Let us now turn to the two small current peaks at higher applied voltages in figure 8. The total energy dependence of the transmission probability calculated at the two peak voltages is shown in figures 11(*a*)–(*d*). Figures 11(*a*) and (*b*) show the diagonal, $|S_{12}(\gamma,\gamma)|^2$, and off-diagonal, $|S_{12}(1,\gamma)|^2$, at the fifth peak voltage, and figures 11(*c*) and (*d*) the diagonal, $|S_{12}(\gamma,\gamma)|^2$, and the off-diagonal, $|S_{12}(2,\gamma)|^2$, at the sixth peak voltage. Small transmission peaks located under the Fermi energy are again found which lead to the fifth and sixth current peaks. These transmission peaks are, however, attributed not to diagonal tunnelling but to off-diagonal tunnelling: lateral-mode-non-conserving resonant tunnelling $1 \rightarrow 5$ for the fifth peak shown in figure 11(*b*) and $2 \rightarrow 9$ for the sixth peak shown in figure 11(*d*). It should be mentioned that, for the sixth current peak, the $3 \rightarrow 10$ tunnelling channel is simultaneously opened with the $2 \rightarrow 9$ channel. As described above, the fourth current peak is mainly due to $5 \rightarrow 5$ and $6 \rightarrow 6$ diagonal tunnelling, along with a small contribution by $1 \rightarrow 5$ off-diagonal tunnelling. Even after the diagonal tunnelling channels close, at a voltage such that the fifth and sixth lateral eigenstates in the quantum well simultaneously line up with the fifth and sixth lateral eigenstates in the cathode region, the off-diagonal channel $1 \rightarrow 5$ is still open, resulting in another current peak. Thus the fifth $1 \rightarrow 5$ peak can be thought of as a satellite peak of the main fourth $5 \rightarrow 5$ peak. However, in the case of the sixth $2 \rightarrow 9$ peak the diagonal $9 \rightarrow 9$ channel cannot give rise to a main peak as the ninth eigenstate in the cathode region is essentially unoccupied, so the $2 \rightarrow 9$ channel gives rise to a new main peak.

As shown here the number of extra current peaks (shoulders) observed in the I–V characteristics directly measures the number of resonant tunnelling channels in which the lateral mode is not conserved. Also it is possible to estimate the magnitude of the lateral-mode mixing by analysing the extra peak current.

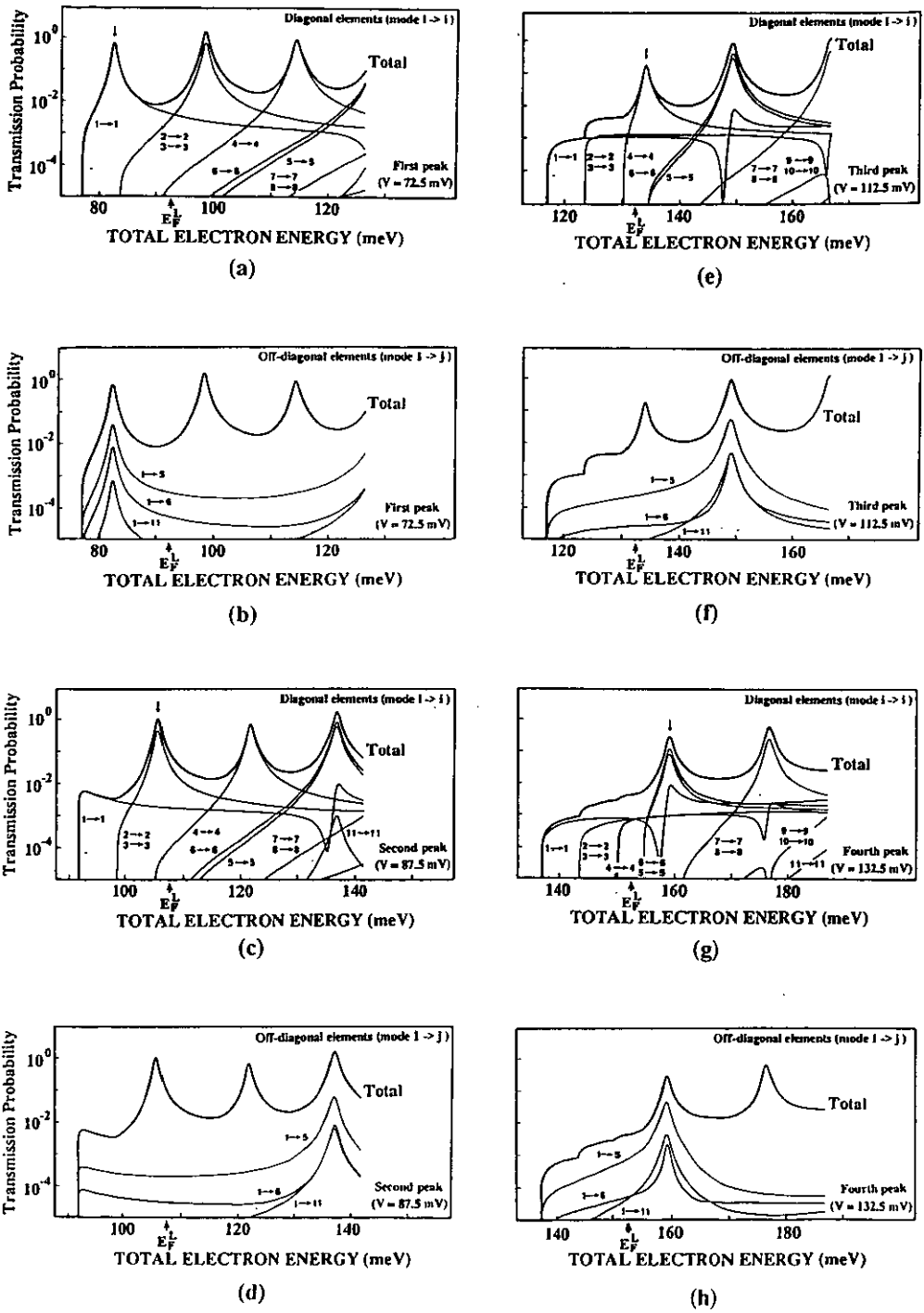

Figure 10. Total energy dependences of the transmission probabilities calculated at the first four peak (shoulder) voltages indicated by arrows with the numbers 1, 2, 3, and 4 in figure 3. (*a*), (*c*), (*e*), and (*g*) show the diagonal elements $|S_{12}(\gamma,\gamma)|^2$ and (*b*), (*d*), (*f*), and (*h*) the off-diagonal elements $|S_{12}(1,\gamma)|^2$. The total transmission rate is shown by using thick full curves as in figures 3 and 4.

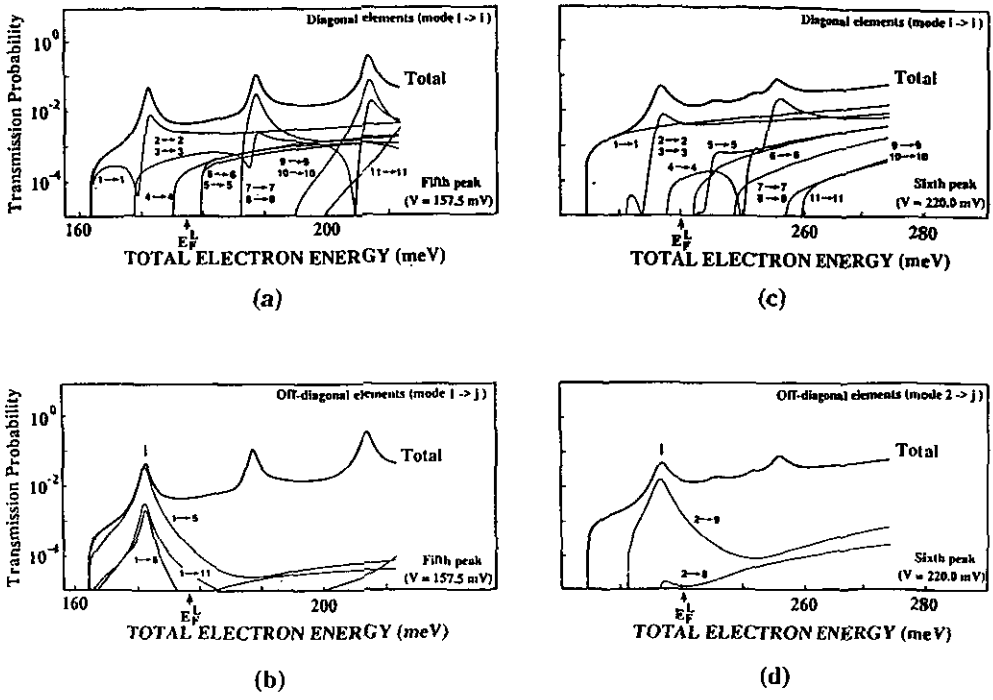

Figure 11. Total energy dependence of the transmission probability calculated at the last two peak voltages indicated by arrows with the numbers 5 and 6 in figure 3. (*a*) and (c) show the diagonal elements $|S_{12}(\gamma, \gamma)|^2$, (*b*) the off-diagonal $|S_{12}(1, \gamma)|^2$, and (*d*) the off-diagonal $|S_{12}(2, \gamma)|^2$.

4. Conclusions

We have reported a numerical simulation of a zero-dimensional resonant tunnelling diode based on three-dimensional S-matrix theory. By taking lateral-mode mixing into consideration, the three-dimensional Schrödinger equation has been solved for an $Al_{0.25}Ga_{0.75}As/In_{0.08}Ga_{0.92}As/Al_{0.25}Ga_{0.75}As$ double-barrier structure with a lateral cross sectional area of 80 nm^2. The effect of lateral-mode mixing, caused by elastic scattering due to the hour-glass-shaped lateral-confinement potential, on the multi-mode transmission properties and the current–voltage characteristics of the device has been analysed quantitatively. Comparisons have been made with a device under entirely uniform confinement.

We have shown that the hour-glass confinement potential causes larger energy intervals between transmission probability peaks and the mixing of lateral modes. These effects result in a large peak-to-valley ratio of transmission probability and the opening of new off-diagonal tunnelling channels, respectively. The calculated S-matrix clearly shows both new transmission peaks in the off-diagonal components, which represent lateral-mode-non-conserving resonant tunnelling, and related Fano-resonance-type structures in the diagonal components, which represent an interference between the second-order resonant tunnelling process and the diagonal tunnelling process under the off-resonant condition. The calculated total tunnelling current through the device shows several small satellite peaks which are superposed on the

conventional negative differential conductance. Analysis of the S-matrix has shown that two of the peaks observed in the higher-applied-voltage regime are caused by resonant tunnelling in which the lateral modes are not conserved.

Acknowledgments

The authors would like to thank K Yamaguchi and K Miyauchi of Central Research Laboratory, Hitachi Ltd for their continuous support and encouragement. The authors also wish to thank their collaborators at Cambridge for many helpful discussions: K Nakazato, D Williams, J Allam, J White, R Blaikie, J R A Cleaver, T Thornton and H Ahmed.

References

[1] Tsu R and Esaki L 1973 Tunneling in a finite superlattice *Appl. Phys. Lett.* **22** 562
[2] Reed M A, Randall J N, Aggarwal R J, Matyi R J, Moore T M and Westel A E 1988 Observation of discrete electronic states in a zero-dimensional semiconductor nanostructure *Phys. Rev. Lett.* **60(6)** 535
[3] Reed M A, Randall J N and Luscombe J H 1990 Non-equilibrium quantum dots: transport *Nanotechnology* 1 63
[4] Tarucha S, Hirayama Y, Saku T and Kimura T 1990 Resonant tunneling through one- and zero-dimensional states constricted by $Al_xGa_{1-x}As/GaAs/Al_xGa_{1-x}As$ heterojunctions and high-resistance regions induced by focused Ga ion-beam implantation *Phys. Rev.* B **41** 5459
[5] Su Bo, Goldman V J, Santos M and Shayegan 1991 Resonant tunneling in submicron double-barrier heterostructures *Appl. Phys. Lett.* **58** 747
[6] Tarucha S and Hirayama Y 1991 Magnetotunneling in a coupled two-dimensional–one-dimensional electron system *Phys. Rev.* B **43** 9373
[7] Dellow M W, Benton P H, Henini M, Main P C, Eaves L, Beaumont S P and Wilkinson C D W 1991 Gated resonant tunneling devices *Electron. Lett.* **27** 134
[8] Gueret P, Blanc N, German R and Rothuizen H 1992 Confinement and single-electron tunneling in Schottky-gated, laterally squeezed double-barrier quantum-well heterostructure *Phys. Rev. Lett.* **68** 1896
[9] Tarucha S, Tokura Y and Hirayama Y 1991 Resonant tunneling of three-dimensional electrons into degenerate zero-dimensional levels *Phys. Rev.* B **44** 13815
[10] Groshev A 1990 Single electron trapping in ultrasmall double barrier semiconductor structures *20th Int. Conf. on Physics of Semiconductors (Thessaloniki, 1990)* (Singapore: World Scientific) p 1238
[11] Groshev A, Ivanov T and Valtchinov V 1991 Charging effects of a single quantum level in a box *Phys. Rev. Lett.* **66** 1082
[12] Stopa M P 1992 Charging energy and collective response of a quantum dot resonant tunneling device *Surf. Sci.* **263** 433
[13] Chou S Y, Wolak E and Harris J S Jr 1988 Resonant tunneling of electrons of one or two degrees of freedom *Appl. Phys. Lett.* **52** 657
[14] Bryant G W 1989 Resonant tunneling in zero-dimensional nanostructures *Phys. Rev.* B **39** 3145
[15] Bryant G W 1991 Understanding quantum-box resonant-tunneling spectroscopy: fine structure at Fermi-level crossings *Phys. Rev.* B **44** 3782
[16] Bryant G W 1991 Nonadiabatic transport through quantum dots *Phys. Rev.* B **44** 12837
[17] Luban M, Luscombe J H, Reed M A and Pursey D L 1989 Anharmonic oscillator model of a quantum dot nanostructure *Appl. Phys. Lett.* **54** 1997
[18] Barker J R 1989 Theory of quantum transport in lateral nanostructures *Nanostructure Physics and Fabrication, Proc. Int. Symp. (Texas, 1989)* (New York: Academic) p 253
[19] Sols F, Macucci M, Ravaioli U and Hess K 1989 Theory of a quantum modulated transistor *J. Appl. Phys.* **66** 3892
[20] Brum J A 1990 Superlattice effects in quantum dots *20th Int. Conf. on Physics of Semiconductors (Thessaloniki, 1990)* vol 3 (Singapore: World Scientific) p 511

[21] Ulloa S E, Castano E and Kirczenow G 1990 Ballistic transport in a novel one-dimensional superlattice *Phys. Rev.* B **41** 12350

[22] Ji Z L and Berggren K F 1991 Numerical study of ballistic conductance in parallel configuration *Semicond. Sci. Technol.* **6** 63

[23] Weisshaar A, Lary J, Goodnick S M and Tripathi V K 1991 Negative differential resistance in a resonant quantum wire structure *IEEE Electron. Device Lett.* **EDL-12** 2

[24] Kumar A and Bagwell P H 1991 Resonant tunneling in a quasi-one-dimensional wire: influence of evanescent modes *Phys. Rev.* B **43** 9012

[25] de Aguiar F M and Wharam D A 1991 Transport through one-dimensional channels *Phys. Rev.* B **43** 9984

[26] Kumar A, Laux S E and Stern F 1990 Electron states in a GaAs quantum dot in a magnetic field *Phys. Rev.* B **42** 5166

[27] Kumar A 1992 Self-consistent calculations on confined electrons in three-dimensional geometries *Surf. Sci.* **263** 335

[28] Nakasato K and Blaikie R J 1991 The effect of mode coupling on ballistic electron transport in quantum wires *J. Phys.: Condens. Matter* **3** 5729

[29] Mizuta H, Yamaguchi K, Yamane M, Tanoue T and Takahashi S 1989 Two-dimensional numerical simulation of Fermi-level pinning phenomena due to DX centers in AlGaAs/GaAs HEMTs *IEEE Trans. Electron. Devices* **ED-36** 2307

[30] Spicer W E, Chye P W, Skeath P R, Su C Y and Lindau I 1979 New and unified model for Schottky barrier and III–V insulator interface states formation *J. Vac. Sci. Technol.* **16** 1422

[31] See, for example,
Press W H, Flannery B P, Teukolsky S A and Vetterling W T 1986 *Numerical Recipes, The Art of Scientific Computing* (Cambridge: Cambridge University Press) p 356

[32] Fano U 1961 Effects of configuration interaction on intensities and phase shifts *Phys. Rev.* **124** 1866